Phys. Status Solidi B **250**, No. 4, 793–800 (2013) / **DOI** 10.1002/pssb.201200817

physica status solidi b
www.pss-b.com
basic solid state physics

Feature Article

First-principles calculations of point defects in inorganic nanotubes

Yuri F. Zhukovskii[*,1], **Sergei Piskunov**[1,2,3], **Jevgenijs Begens**[1], **Jurijs Kazerovskis**[1], **and Oleg Lisovski**[1]

[1] Institute for Solid State Physics, University of Latvia, Kengaraga 8, Riga LV-1063, Latvia
[2] Faculty of Physics and Mathematics, University of Latvia, Zellu 2, Riga LV-1002, Latvia
[3] Faculty of Computing, University of Latvia, 19 Raina Blvd., Riga LV-1586, Latvia

Received 9 October 2012, revised 29 October 2012, accepted 30 October 2012
Published online 20 March 2013

Keywords DFT calculations, electronic structure, inorganic nanotubes, morphology, point defects, single-walled nanotubes

* Corresponding author: e-mail quantzh@latnet.lv, Phone: +371-67-187816, Fax: +371-67-132778

The first-principles calculations have been performed to investigate the ground-state properties of monoperiodic boron nitride (BN), TiO_2, and $SrTiO_3$ single-walled nanotubes (SW NTs) containing extrinsic point defects. The hybrid exchange–correlation functionals PBE, B3LYP, and B3PW within the framework of density functional theory (DFT) have been applied for large-scale *ab initio* calculations on NTs with the following substitutional impurities: Al_B, P_N, Ga_B, As_N, In_B, and Sb_N in the BN NT, as well as C_O, N_O, S_O, and Fe_{Ti} in the TiO_2 and $SrTiO_3$ NTs, respectively. The variations in formation energies obtained for equilibrium defective nanostructures allow us to predict the most stable compositions, irrespective of the changes in growth conditions. The changes in the electronic structure are analyzed to show the extent of localization of the midgap states induced by defects. Finally, the electronic charge redistribution was calculated in order to explore the intermolecular properties, which show how the reactivity of the NTs under study was affected by doping and orbital hybridization.

1 Introduction Inorganic nanotubes (NTs) are important and widespread materials in modern nanotechnology. Moreover, imperfect NTs with reproducible distribution of point defects attract enhanced interest, due to potential generation of novel innovative nanomaterials and devices. A variety of experimental conditions accompanying their synthesis can certainly promote the appearance of point defects: native vacancies or antisites as well as substitutional impurities. These and other types of irregularities may occur in inorganic NTs as a result of the growth process or intentionally induced to modify their properties. Point defects also play the role of chemically active sites for NT-wall functionalization [1].

Boron nitride (BN), titania (TiO_2), and strontium titanate ($SrTiO_3$ or STO) are well-known semiconductors comprehensively studied in materials science, thanks to their widespread technological applications. During recent years NTs of different morphology obtained from these compounds were systematically synthesized and carefully studied as prospective technological materials (see *e.g.*, Refs. [2, 3] for BN, Ref. [4] for TiO_2, and Ref. [5] for STO). The doped BN NTs, which exhibit substantial changes in electronic properties with respect to their pristine counterparts, further enlarge applications in the nanosize range. For example, either a single boron or a single nitrogen atom substituted in the C-doped BN NTs was found to induce spontaneous magnetization [6], while an insulator-to-semiconductor transition has been observed on the successfully synthesized F-doped BN NTs [7]. Very recent experimental studies performed on Nb-doped TiO_2 NTs, fabricated by anodization of Ti–Nb alloys [8], and Gd^{3+}–N codoped trititanate NTs prepared using the hydrothermal method [9] demonstrate strongly enhanced photoelectrochemical water splitting without considerable photodegradation. Analogously, STO NTs after doping are potentially promising photoelectrodes for visible-light-driven photocatalytic applications [10, 11].

In spite of large (mainly experimental) efforts the current understanding of fundamental changes in electronic structure with atomic composition of doped semiconducting NTs is still insufficient to rationally design the atomic composition of these prospective nanomaterials. To guide the search, a theoretical prediction is needed to prudently suggest the electronic structure and charge transition in

tubular nanostructured materials. Although point defects in BN NTs are much better described from the theoretical point of view (see Refs. [1, 3] and references therein), the extrinsic isoelectronic substitutional impurities in BN NT walls [12] were not sufficiently studied from first principles. Theoretical simulations performed so far dealt, *e.g.*, with doped and codoped TiO_2 [13, 14] and STO [15, 16] bulk, as well as titania anatase- and rutile-type low-index surfaces (101) and (110), respectively [17, 18], or nanoparticles [19]. However systematic theoretical studies performed on doped semiconducting metal-oxide NTs are rather scarce in the literature.

In this paper, we continue to present a series of results obtained using *ab initio* simulations on both perfect and defective BN NTs [20–23], as well as on perfect TiO_2 and STO NTs [24–27]. Using hybrid exchange–correlation functionals applied within the density functional theory (DFT) we have calculated the following extrinsic isoelectronic substitutional impurities in BN NT: Al_B, P_N, Ga_B, As_N, In_B, and Sb_N as they may produce a strong effect in the luminescence spectra of nanostructured BN [12]. Moreover, C_O, N_O, S_O, and Fe_{Ti} extrinsic substitutional impurities in the TiO_2 and $SrTiO_3$ NTs have been calculated too since they essentially enhance photocatalytic activity of both NT types [28]. The calculated changes in the electronic structure of nanomaterials under study, *e.g.*, the electronic charge redistribution around substitutional defects, are thoroughly discussed.

The paper is organized as follows. In Section 2, the computational details of first-principles calculations are described. Section 3 presents the calculated electronic properties, *e.g.*, electronic charge redistribution around extrinsic substitutional point defects in the aforementioned NTs. Finally, a short summary is given in Section 4.

Yuri Zhukovskii obtained his B.Sc. and M.Sc. degrees from the Department of Physics and Mathematics at the University of Latvia, Riga. In 1993, he gained the Ph.D. degree (Dr. Chem.) from Institute of Inorganic Chemistry, Latvian Academy of Sciences, Latvia, and Institute of Physics, St. Petersburg State University, Russia, for his thesis "Quantum-chemical study of water chemisorption on aluminum surface". Between 1995 and 2007, he was Fellow at the Helsinki University of Technology, Espoo (Finland), the University of Western Ontario, London (ON, Canada), and the Northwestern University, Evanston (IL, USA). Dr. Zhukovskii has extended teaching experience and has participated in several international research activities, among them the EC Framework 7 Project on Nanoscale ICT Devices and Systems, the EUROATOM ACTINET networking Project on Nuclear Fuels, and the FP 7 Marie Curie CACOMEL Project (Nano-carbon based components and materials for high frequency electronics). From 2012 he is Head of the Laboratory of Computer Modeling of the Electronic Structure of Solids at the Institute of Solid State Physics at University of Latvia, Riga. His main research interests include the physics and chemistry of crystalline solids, surface science, adsorption and surface reactivity, physics and chemistry of nanostructures, quantum chemistry, and computational materials science.

2 Computation details Rather scarce results were reported so far on computer simulations of realistic defective NTs since the lack of periodicity makes their calculations space- and time-consuming. In this study, we have performed the first-principles simulations on doped NTs using the formalism of the localized Gaussian-type functions (GTFs), which form the basis set (BS), and exploiting periodic rototranslation symmetry for efficient ground-state calculations as implemented in the *ab initio* code CRYSTAL developing the formalism of localized atomic orbitals (LCAO) for calculations on periodic systems [29]. Earlier, this approach was successfully applied by us for simulations on single- (SW) and multiwalled BN, TiO_2, and STO NTs [20–27].

We employ the hybrid exchange–correlation scheme that accurately reproduces the basic bulk and surface properties of BN [20–22] as well as a number of perovskites [30–32]. Our calculations on defective BN NTs have been performed using the hybrid Hartree–Fock/Kohn–Sham (HF/KS) exchange–correlation functional PBE0 of Perdew–Becke–Erzerhof [33, 34] combining exact HF nonlocal exchange and KS exchange operator within the generalized gradient approximation (GGA) as implemented in CRYSTAL code [29]. For calculations on defective TiO_2 and STO NTs we have employed the hybrid B3LYP and B3PW exchange–correlation functional, respectively. They consist of the nonlocal HF exchange, DFT exchange, and GGA correlation functionals as proposed by Becke [35]. The main advantage of the hybrid DFT calculations is that they make the results of the band-structure calculations more plausible.

To perform calculations, the following configurations of BSs have been adopted. An all-valence BS in the form of 6s–21sp–1d and 6s–31p–1d has been used for B and N atoms, respectively [22]. For substitutional impurity atoms in BN NTs, the 21sp–1d BSs with an effective core pseudopotential (ECP) from Durand and coworkers [36–38] have been used. For Sr and Ti atoms in TiO_2 and STO NTs, the BSs have been chosen in the form of 311sp–1d and 411sp–311d, respectively, using ECP from Hay and Wadt [39], while full-electron BSs were adopted for all other atoms in calculations of defective titania and strontium titanate NTs, *i.e.*, O: 8s–411sp–1d; C: 6s–411sp–11d; N: 6s–31p–1d, S: 8s–63111 sp-11d, and Fe: 8s–6411 sp–41d (see Refs. [29, 40]).

To provide the balanced summation over the direct and reciprocal lattices of BN NT, the reciprocal-space integration has been performed by sampling the Brillouin zone (BZ) with the $10 \times 1 \times 1$ Pack–Monkhorst *k*-mesh [41] that

results in six eventually distributed k-points at the segment of irreducible BZ. Extended 2×2 supercells have been used to simulate quasi-isolated point defects in TiO_2 and STO NTs. Therefore, BZ sampling for these NTs have been chosen with the $6 \times 1 \times 1$ Pack–Monkhorst k-mesh or four k-points per segment. Threshold parameters of CRYSTAL code (ITOLn) for evaluation of different types of bielectronic integrals (overlap and penetration tolerances for Coulomb integrals, ITOL1 and ITOL2, overlap tolerance for exchange integrals ITOL3, as well as pseudo-overlap tolerances for exchange integral series, ITOL4 and ITOL5) [29] have been set to 8, 8, 8, 8, and 16, respectively. (If the overlap between the two atomic orbitals is smaller than $10^{-\mathrm{ITOLn}}$, the corresponding integral is truncated.) Truncation parameters in the case of TiO_2 and STO NTs have been set to 7, 8, 7, 7, and 14, respectively. Further increase of k-mesh and threshold parameters results in much more expensive calculations, yielding only a negligible gain in the total energy ($\sim 10^{-7}$ a.u.). Calculations are considered as converged when the total energy obtained in the self-consistent field procedure differs by less than 10^{-7} a.u. in the two successive cycles. Effective charges on atoms as well as net bond populations have been calculated according to the Mulliken population analysis [29].

Equilibrium lattice constants calculated for the bulk of hexagonal BN have been found to be qualitatively close to their experimental values (a_0 of 2.51 vs. 2.50 Å obtained in experiment and b_0 of 7.0 vs. 6.7 Å [42]), thus, indicating reliable geometry optimization of BN BSs. The optical bandgap (δ) measured experimentally for hexagonal BN bulk is 5.96 eV [43], the value of δ calculated by us is found to be somewhat overestimated (6.94 eV), which is rather typical of hybrid methods considered in the current study. The value of δ calculated for bulk TiO_2 in anatase phase yields 3.64 vs. 3.18 eV in experiment, while δ calculated for bulk STO in high-symmetry cubic phase yield 3.63 vs. 3.25 eV. A reasonable agreement between measured and calculated equilibrium lattice constants of both TiO_2 and STO bulk solids is also obtained (see Refs. [27] and [40]).

The formation energies of a single substitutional impurity defect A_h in NTs have been estimated as follows:

$$E^{\mathrm{form}}_{A_h} = E^{\mathrm{tot}}_{A_h/\mathrm{NT}} + E^{\mathrm{tot}}_{h} - E^{\mathrm{tot}}_{A_h} - E^{\mathrm{tot}}_{\mathrm{NT}}, \quad (1)$$

where $E^{\mathrm{tot}}_{A_h/\mathrm{NT}}$ is the calculated total energy of an NT containing substitutional impurity defect A_h, E^{tot}_{h} is the total energy of the host atom removed from the NT, $E^{\mathrm{tot}}_{A_h}$ is the total energy calculated for the impurity atom, and $E^{\mathrm{tot}}_{\mathrm{NT}}$ stands for the total energy calculated for the ideal NT.

3 Results and discussion

3.1 Al_B-, Ga_B-, In_B-, P_N-, As_N-, and Sb_N-doped BN nanotubes The first principles method employed for this study allows us to describe 1D NTs in their original space form. The approach that allows BN NT formation starting from an hexagonal BN bulk and a (0001) monolayer, which is similar to the hexagonal structure of graphite bulk and graphene nanosheet, respectively, in accordance with a model of structural transformation (3D → 2D → 1D) [44] as described elsewhere [22]. Using this approach we have constructed the monoperiodic unit cell of ideal BN NTs of armchair type with chirality indexes (5,5). To achieve a dilute limit of a single substitutional point defect, we have built a $3 \times 1 \times 1$ supercell having an interdefect distance as large as 7.5 Å with 60 atoms in the periodically repeated unit cell. The defective nanostructures have been modeled by host B or N atom substitution by the impurity atom A_h, *i.e.*, Al_B, Ga_B, In_B, P_N, As_N, and Sb_N (Fig. 1). The coordinates of all atoms of each nanostructure containing substitutional point defect have been optimized using the PBE0-DFT method as implemented in the CRYSTAL code [29].

Analysis of equilibrium distances between substitutional defect and host atoms clearly demonstrates that the bond length of a substitutional impurity defect, A_h, and closest host atoms of BNNT, h'_n, tend to elongate with respect to the B–N bond length of pristine BNNT (1.45 Å). The bond length $l_{A_h-h'_n}$ increases along with increasing atomic mass of the substitutional defect atom, *i.e.*, $l_{Al_B-N_1} = 1.73$ Å vs. $l_{In_B-N_1}$ of 1.97 Å. We note also the outward relaxation of the host BNNT atoms nearest to the A_N substitutional atoms that is noticeably larger than that in the case of A_B substitutional defects: *i.e.*, $l_{Ga_B-N_1} = 1.80$ Å, while $l_{As_N-B_1} = 2.07$ Å. Obviously, due to a partial covalency of B–N bonds, atoms can be more easily rearranged around the substitutional point defect. In the case of A_N substitutional atoms, they are displaced outwards to the NT wall. Such a relaxation is accompanied by slightly increased covalency along with extra charge redistribution (see the enhanced charge-density redistribution shown in Fig. 2). The increase of covalency is confirmed by the calculated effective Mulliken charges on extrinsic substitutional defects: $1.01e$ (Al_B), $-0.34e$ (P_N), $1.41e$ (Ga_B), $-0.56e$ (As_N), $1.33e$ (In_B), and $-0.32e$ (Sb_N).

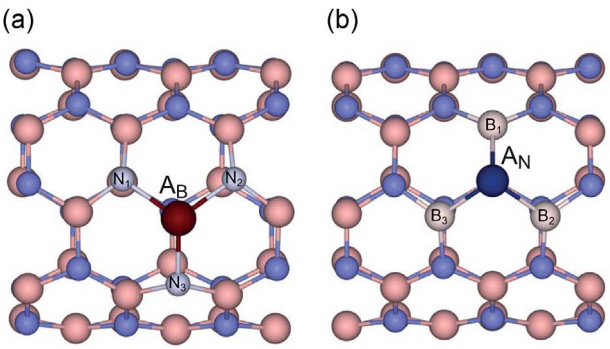

Figure 1 (online color at: www.pss-b.com) Schematic representation of monoperiodically repeated unit cell of the substitutional defect containing (5,5) BN NT with an external diameter of 0.69 nm: (a) host boron substitutes for impurity defect atom (A_B) and (b) host nitrogen substitutes for impurity defect atom (A_N). Borons are shown as blue (dark gray) balls, while nitrogens as pink (light gray) ones. Host atoms nearest to defect neighbor (h'_n) are shown in dimmed colors.

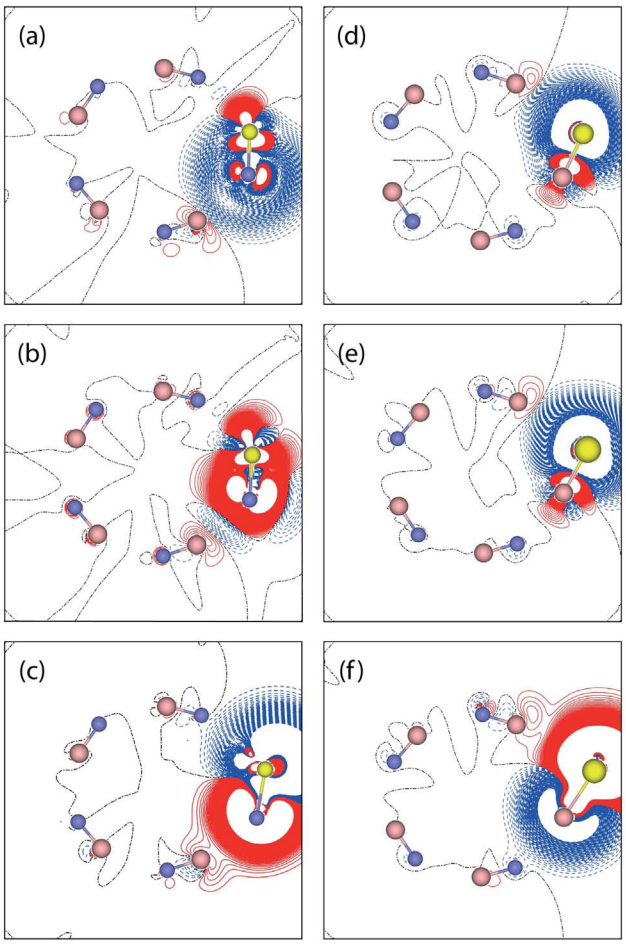

Figure 2 (online color at: www.pss-b.com) 2D difference electron-density plots $\Delta\rho(\mathbf{r})$ (the sum of total electron densities in the defective BN NT and isolated host B (or N) atom minus the sum of these densities in the isolated impurity atom (A_h, where h stands for "host" atom) and perfect NT) projected onto the section planes across BN NT containing an impurity defect per supercell (Fig. 1): (a) Al_B/BNNT, (b) Ga_B/BNNT, (c) In_B/BNNT, (d) P_N/BNNT, (e) As_N/BNNT, (f) Sb_N/BNNT. Borons are shown as blue (dark gray) balls, nitrogens as pink (light gray) balls, substitutional impurity atoms (A_h) are shown in yellow (light gray). Dash-dotted (black) isolines correspond to the zero level. Solid (red) and dashed (blue) isolines describe positive and negative values of the difference electron density, respectively. Isodensity curves are drawn from -0.01 to $+0.01 e\text{Å}^{-3}$ with an increment of $0.0001\, e\text{Å}^{-3}$.

The formation energies of a single substitutional point defect onto relaxed BNNT have been found to increase along with atomic mass of substitutional defect. Calculated formation energies of Al_B and P_N substitutes can be compared (4.37 and 4.86 eV, respectively), while As_N and Sb_N appear to be more energetically stable with respect to Ga_B and In_B.

Although BNNT has been calculated for the interdefect distance of 7.5 Å, the interaction between the adjacent defects has been found to be negligible. In the current study, the energy dispersion of the populated defect levels in band structures of defective BNNTs does not exceed 0.02 eV, thus, they look like straight lines. In the case of undoped BNNT its top of the valence band (VB) consists of boron 2p orbitals, while its bottom of the conduction band (CB) consists of nitrogen 2p orbitals. In our study we have calculated the projected density of states (PDOSs) for all nanostructures considered. In the case of Al_B/BNNT the top of the VB is localized on B(2p) orbitals with the bottom of the CB formed by 3p orbitals of Al impurity atom localized slightly below the bottom of the CB of an ideal BNNT yielding a bandgap of 6.42 eV. In the case of Ga_B/BNNT the Ga(4p) defect level splits out ~2 eV below the CB, yielding the bandgap of 5.02 eV. In the case of In_B/BNNT the In(5p) defect level splitting is much more pronounced with the bandgap of 3.55 eV. For the N substitutional defects the p states of impurity atoms contribute to the top of the VB inducing the defect levels in the vicinity of the CB bottom formed mainly by 2p orbitals of the nearest host nitrogens. Their influence on the bandgap of defective BNNTs is more modest with respect to the B substitutional defects. The P_N/BNNT yield the bandgap of 6.24 eV, As_N/BNNT has the bandgap of 5.94 eV and a bandgap of 5.03 eV has been calculated for Sb_N/BNNT.

3.2 C_O-, N_O-, S_O-, and Fe_{Ti}-doped TiO_2 nanotubes In Ref. [27], we have calculated energetics for TiO_2 NTs folded from nanosheets and having diameters ranging from 0.6 to 4 nm. The purpose of this was to define the most energetically stable TiO_2 NT. According to our calculations, 9-layered (001) NT with (0,n) chirality indexes possess negative strain energy, *i.e.*, it is energetically more favorable to form an NT rather than to keep the original 2D structure. It is worth mentioning that our prediction is in good agreement with an earlier theoretical study performed by Ferrari et al. [45]. Based on our strain energy calculations, we have chosen for further substitutional doping 2×2 supercell of a (0,36) 9-layered anatase (001) NT with internal diameter of 3.47 nm, a wall thickness of 0.67 nm, and having 648 atoms in the unit cell (Fig. 3). Oxygen substitutional impurities have replaced host atoms in six possible configurations, while three possible substitutional positions have been available for Fe_{Ti} (Fig. 3). Thus, the overall defect concentration in TiO_2 NT is ~8%. In this paper we discuss only the substitutional impurities with the lowest energy of formation: C_{O_1}/TiO_2 NT with $E_{form} = 1.16$ eV, N_{O_2}/TiO_2 NT with $E_{form} = 3.56$ eV, S_{O_1}/TiO_2 NT with $E_{form} = 2.61$ eV, and Fe_{Ti_3}/TiO_2 NT with $E_{form} = 5.37$ eV.

The electronic charge redistributions induced by the extrinsic impurity defects TiO_2 NT are shown in Fig. 4. In the charge-density maps one can observe considerably larger charge delocalization across the NT. This can be explained by a more expressed reconstruction of the atomic coordination spheres nearest to a defect. Additionally, it should be emphasized that the defect–host atom bonds are saturated, which gives rise to an increase of covalency. Effective Mulliken charges calculated for extrinsic substitutional

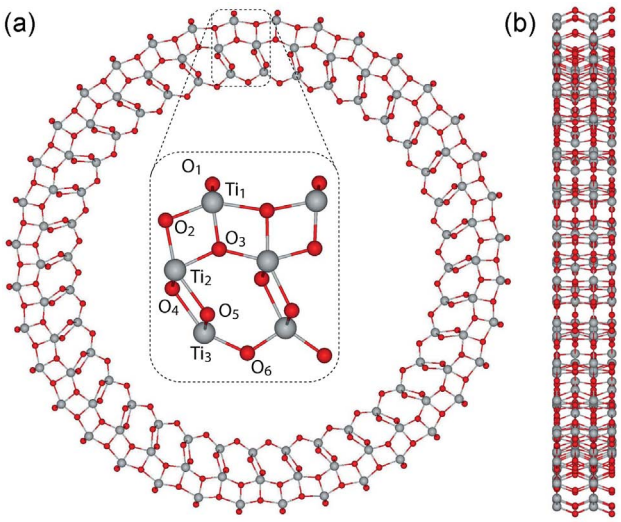

Figure 3 (online color at: www.pss-b.com) Schematic representation of monoperiodically repeated unit cell of the substitutional defect containing (0,36) TiO_2 NT with an external diameter of 4.81 nm: (a) cross-sectional view, (b) side view. Ti are shown as gray balls, and oxygen as red (dark gray) ones. Inset shows the 2×2 increased "basic" unit cell of (0,36) TiO_2 NT repeated by 18 rototranslational symmetry operators (rotation axis of 18th order). Numbered atoms of titanium and oxygen are substituted for impurity defect atoms (A_h, where h stands for "host").

defects in TiO_2 NT have been found to be: $-1.00e$ (C_{O_1}), $-1.06e$ (N_{O_2}), $-1.12e$ (S_{O_1}), and $2.17e$ (Fe_{Ti_3}). Mulliken charges calculated for host Ti and O atoms along the wall of TiO_2 NTs are $2.25e$ and $-1.19e$, respectively.

Band structures calculated for TiO_2 NTs containing substitutional point defects reveal the tendency of the formation of defect-induced levels inside the optical bandgap. In the case of C_{O_1}/TiO_2 NT the filled band is positioned ~0.9 eV below the bottom of the CB, while in the case of N_{O_2}/TiO_2 NT impurity the induced level is found to be close to the bottom of the CB and, thus, gives rise to conductivity. The defect-induced level calculated for S_{O_1}/TiO_2 NT is located ~1 eV above the top of the VB, and in the case of Fe_{Ti_3}/TiO_2 NT the vacancy-induced level is positioned in the middle of the bandgap. The top of the VB in the case of perfect TiO_2 NT is formed by O 2p orbitals, while the bottom of the CB consists of Ti 3d states.

3.3 C_O-, N_O-, S_O-, and Fe_{Ti}-doped $SrTiO_3$ nanotubes In this study, we consider STO NTs with (18,0) chirality indexes (see Fig. 5) rolled up from a nanosheet cut parallel to (110) surface of bulk STO. This NT possesses negative strain energy and has been found to be the most energetically stable with respect to the STO bulk [26]. Its 2×2 supercell consists of 180 atoms and allows for doping with impurities that do not interact with themselves. Oxygen substitutional impurities have replaced host oxygen in three

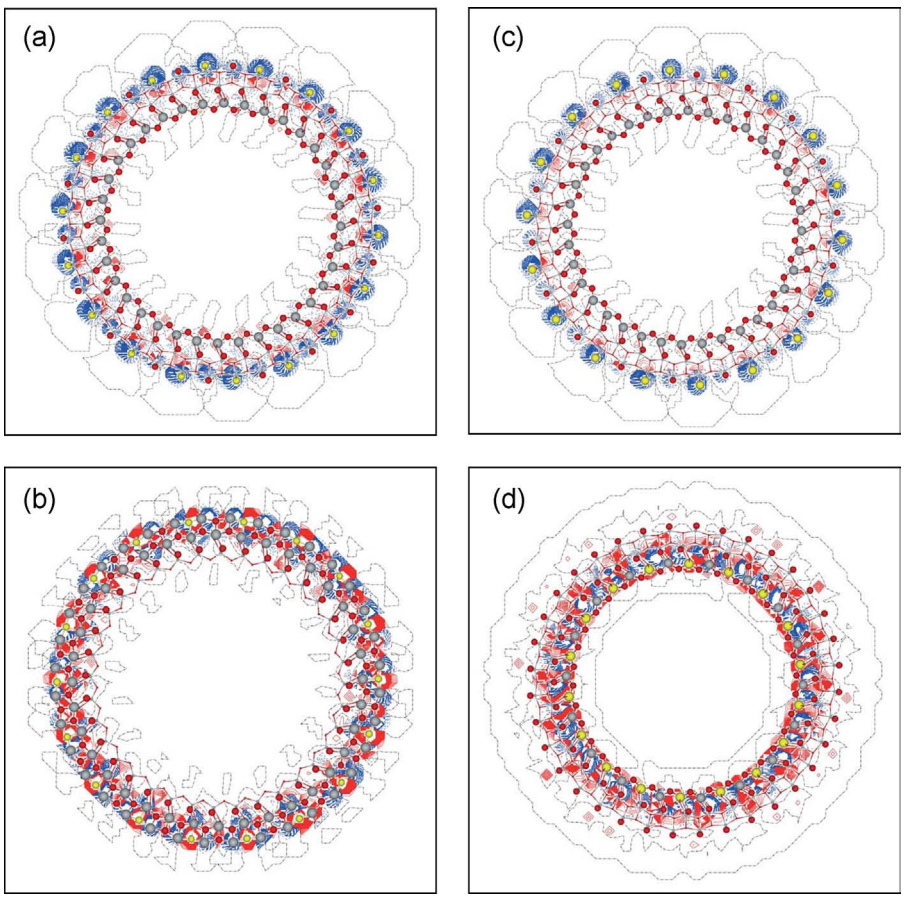

Figure 4 (online color at: www.pss-b.com) 2D difference electron-density plots $\Delta\rho(\mathbf{r})$ (the sum of total electron densities in the defective TiO_2 NT and isolated host Ti (or O) atom minus the sum of these densities in the isolated impurity atom (A_h, where h stands for "host" atom) and perfect NT) projected onto the section planes across the TiO_2 NT containing an impurity defect per supercell (Fig. 3): (a) C_{O_1}/TiO_2 NT, (b) N_{O_2}/TiO_2 NT, (c) S_{O_1}/TiO_2 NT, (d) Fe_{Ti_3}/TiO_2 NT. Ti atoms are shown as gray balls, O as red (dark gray) balls, substitutional impurity atoms (A_h) are shown in yellow (light gray). Atoms positioned outside the crossing plane are shown as balls with reduced size. Dash-dotted (black online) isolines correspond to the zero level. Solid (red) and dashed (blue) isolines describe positive and negative values of the difference electron density, respectively. Isodensity curves are drawn from -0.05 to $+0.05\,e\text{Å}^{-3}$ with an increment of $0.0005\,e\text{Å}^{-3}$.

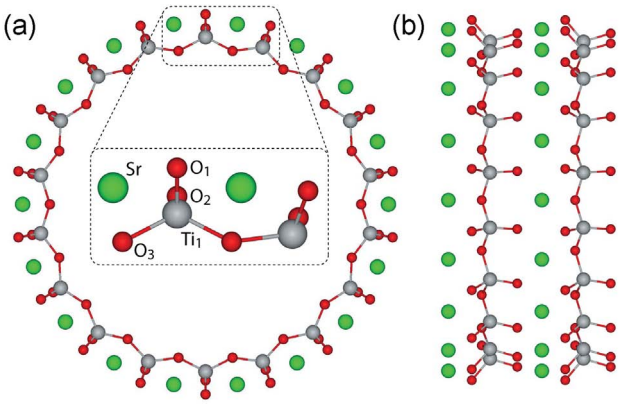

Figure 5 (online color at: www.pss-b.com) Schematic representation of monoperiodically repeated unit cell of the substitutional defect containing (18,0) $SrTiO_3$ NT with external diameter 2.27 nm: (a) front view, (b) side view. Ti are shown as gray balls, oxygens as red (dark gray) balls, and strontiums as green (gray) ones. Inset shows the 2×2 increased "basic" unit cell of (18,0) $SrTiO_3$ NT repeated by 9 rototranslational symmetry operators (rotation axis of the 9th order). Numbered atoms are titanium and oxygen that are substituted for impurity defect atoms (A_h, where h stands for "host").

possible configurations, while only one possible substitutional position has been considered for Fe_{Ti} (Fig. 5). Thus, the overall defect concentration in TiO_2 NT is ~25%. In this paper, we discuss only the substitutional impurities with the lowest energy of formation: $C_{O_3}/SrTiO_3$ NT with $E_{form} = 4.50$ eV, $N_{O_3}/SrTiO_3$ NT with $E_{form} = 3.52$ eV, $S_{O_1}/SrTiO_3$ NT with $E_{form} = 2.01$ eV, and $Fe_{Ti_1}/SrTiO_3$-NT with $E_{form} = 5.97$ eV.

The electronic charge redistributions of STO NT containing extrinsic substitutional defects are shown in Fig. 6. Significant reconstruction of the NT after doping results in the change of a Ti–A_h or Fe–O bond of the perovskite oxygen octahedron (see Fig. 6). This leads to the formation of considerably longer Ti–A_h or Fe–O and accompanied by a change of effective charges and an increase of covalency (bond population) relative to the bulk STO. Effective Mulliken charges calculated for extrinsic substitutional defects in TiO_2 NT have been found to be: $-1.21e$ (C_{O_3}), $-1.13e$ (N_{O_3}), $-1.44e$ (S_{O_1}), and $2.15e$ (Fe_{Ti_1}). Mulliken charges calculated for host Ti and O atoms along the wall of TiO_2 NTs are $2.19e$ and $-1.27e$, respectively.

The PDOSs calculated for the defective STO NTs shows that the top of their VB and the bottom of their CB consist of O 2p and Ti 3d orbitals, respectively, as in bulk STO.

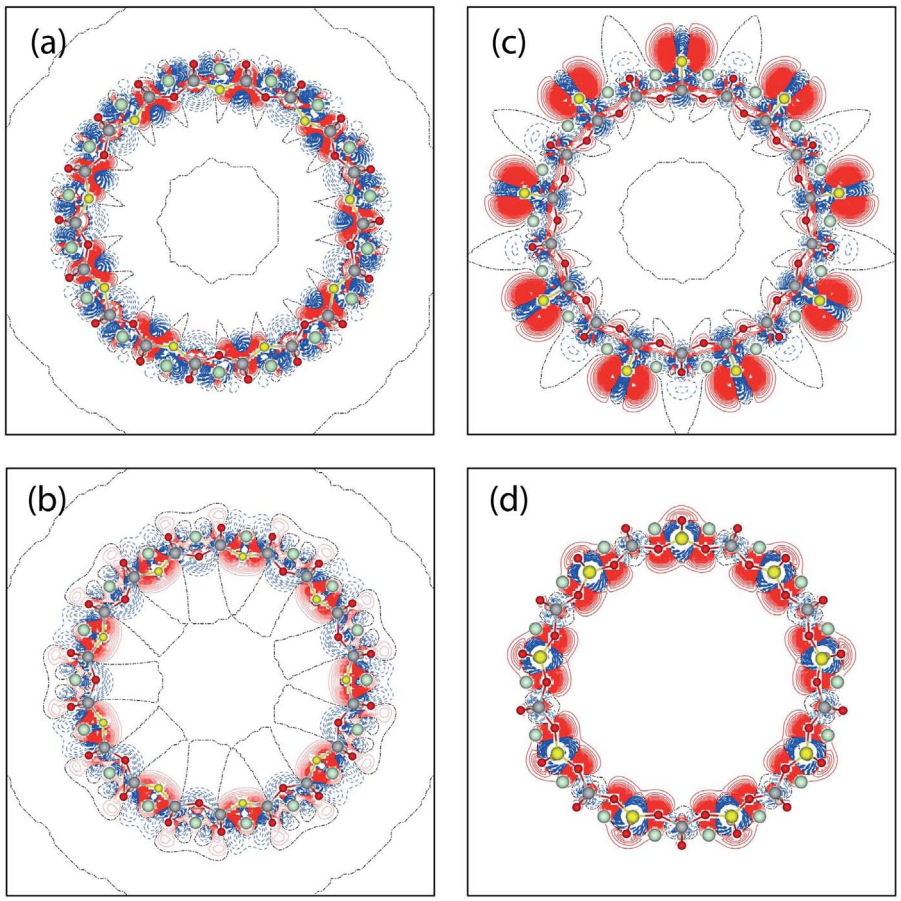

Figure 6 (online color at: www.pss-b.com) 2D difference electron-density plots $\Delta\rho(\mathbf{r})$ (the sum of total electron densities in the defective $SrTiO_3$ NT and isolated host Ti (or O) atom minus the sum of these densities in the isolated impurity atom (A_h, where h stands for "host" atom) and perfect NT) projected onto the section planes across $SrTiO_3$ NT containing an impurity defect per supercell (Fig. 5): (a) $C_{O_3}/SrTiO_3$ NT, (b) $N_{O_3}/SrTiO_3$ NT, (c) $S_{O_1}/SrTiO_3$ NT, (d) $Fe_{Ti_1}/SrTiO_3$ NT. Ti are shown as gray balls, O as red (dark gray) balls, Sr as green (gray), substitutional impurity atoms (A_h) are shown in yellow (light gray). Atoms that are placed outside the crossing plane are shown in dimmed colors. Dash-dotted (black online) isolines correspond to the zero level. Solid (red) and dashed (blue) isolines describe positive and negative values of the difference in electron density, respectively. Isodensity curves are drawn from -0.05 to $+0.05\ e\text{Å}^{-3}$ with an increment of $0.0005\ e\text{Å}^{-3}$.

However, quantum confinement widens the NT's bandgap ($\delta = 5.18$ eV), which means that doping of NTs may lead to the formation of defect states in the bandgap, and thus, to a wider bandgap. This provides additional freedom for bandgap engineering, due to the growing number of mid-gap defect levels. Band-structure calculations for STO NTs containing substitutional point defects reveal the tendency of the formation of defect-induced levels inside the optical bandgap. In the case of C_{O_3}/STO NT the filled band is positioned ~1.5 eV below the bottom of the CB, while in the case of N_{O_3}/STO NT, the impurity-induced level is found to be ~1.5 eV below the bottom of the CB. The defect-induced level calculated for S_{O_1}/STO NT is localized ~4.3 eV above the top of the VB, while in the case of Fe_{Ti_1}/STO NT the vacancy-induced level is positioned just ~1.1 eV below the bottom of the CB.

4 Summary and conclusions In this study, we have presented the results of defect-engineering modeling of boron nitride, titanium dioxide, and strontium titanate nanotubes (NTs) using first-principles calculations based on hybrid DFT. The variations in formation energies obtained for equilibrium defective nanostructures allow us to predict the most stable compositions, irrespective of the changes in growth conditions. Calculated charge–density maps of the different tubular nanostructures containing extrinsic substitutional impurity atoms highlighted changes in the charge distribution caused by doping. This means that the increased covalency in defect–host atom bonds may lead to an enhancement of adsorption properties. This would imply that defective NTs can be used in gas-sensing devices.

On the basis of the performed first-principles calculations, one may conclude that the presence of isoelectronic impurities significantly affects the band structure of the NTs under study, which must be taken into account when constructing nanoelectronic devices based on these NTs. All the mentioned effects can be observed by optical and photoelectron spectroscopy methods, as well as by measuring the electrical properties of the NTs. Midgap levels positioned inside the optical bandgap of defective NTs make them attractive for bandgap engineering in, for example, photocatalytic applications.

Acknowledgements This work has been supported through the ESF project Nr.2009/0216/1DP/1.1.1.2.0/09/APIA/VIAA/044. The authors are thankful to P. N. D'yachkov, R. A. Evarestov, and E. Spohr for stimulating discussions.

References

[1] A. V. Krasheninnikov and K. Nordlund, J. Appl. Phys. **107**, 071301 (2010).
[2] D. Golberg, Y. Bando, Y. Huang, T. Terao, M. Mitome, C. Tang, and C. Zhi, ACS Nano **4**, 2979–2993 (2010).
[3] C. Zhi, Y. Bando, C. Tang, and D. Golberg, Mater. Sci. Eng. R **70**, 92–111 (2010).
[4] P. Roy, S. Berger, and P. Schmuki, Angew. Chem., Int. Ed. **50**, 2904–2939 (2011).
[5] X. Zhu, Z. Liu, and N. Ming, J. Mater. Chem. **20**, 4015–4030 (2010).
[6] R. Q. Wu, L. Liu, G. W. Peng, and Y. P. Feng, Appl. Phys. Lett. **86**, 122510 (2005).
[7] L. Lai, W. Song, J. Lu, Z. Gao, S. Nagase, M. Ni, W. N. Mei, J. Liu, D. Yu, and H. Ye, J. Phys. Chem. B **110**, 14092–14097 (2006).
[8] C. Das, P. Roy, M. Yang, H. Jha, and P. Schmuki, Nanoscale **3**, 3094–3096 (2011).
[9] H. Liu, G. Liu, G. Xie, M. Zhang, Z. Hou, and Z. He, Appl. Surf. Sci. **257**, 3728–3732 (2011).
[10] X. Zhang, K. Huo, L. Hu, Z. Wu, and P. K. Chu, J. Am. Ceram. Soc. **93**(9), 2771–2778 (2010).
[11] J. Zhang, J. H. Bang, C. Tang, and P. V. Kamat, ACS Nano **4**, 387–395 (2010).
[12] P. N. D'yachkov and D. V. Makaev, J. Phys. Chem. Solids **70**, 180–185 (2009).
[13] M. Khan, J. Xu, N. Chen, and W. Cao, J. Alloys Compd. **513**, 539–545 (2012).
[14] M. Li, J. Zhang, and Y. Zhang, Chem. Phys. Lett. **527**, 63–66 (2012).
[15] W. J. Shi and S. J. Xiong, Phys. Rev. B **84**, 205210 (2011).
[16] R. Evarestov, E. Blokhin, D. Gryaznov, E. A. Kotomin, R. Merkle, and J. Maier, Phys. Rev. B **85**, 174303 (2012).
[17] M. Nolan, Phys. Chem. Chem. Phys. **13**, 18194–18199 (2011).
[18] A. M. Márquez, J. J. Plata, Y. Ortega, and J. Fernandez Sanz, J. Phys. Chem. C **115**, 16970–16976 (2011).
[19] S. A. Shevlin and S. M. Woodley, J. Phys. Chem. C **114**, 17333–17343 (2010).
[20] Y. F. Zhukovskii, S. Bellucci, S. Piskunov, L. Trinkler, and B. Berzina, Eur. Phys. J. B **67**, 519–525 (2009).
[21] Y. F. Zhukovskii, S. Piskunov, N. Pugno, B. Berzina, L. Trinkler, and S. Bellucci, J. Phys. Chem. Solids **70**, 796–803 (2009).
[22] R. A. Evarestov, Y. F. Zhukovskii, A. V. Bandura, and S. Piskunov, J. Phys. Chem. C **114**, 21061–21069 (2010).
[23] R. A. Evarestov, Y. F. Zhukovskii, A. V. Bandura, S. Piskunov, and M. V. Losev, J. Phys. Chem. C **115**, 14067–14076 (2011).
[24] R. A. Evarestov, A. V. Bandura, M. V. Losev, S. Piskunov, and Y. F. Zhukovskii, Physica E **43**, 266–278 (2010).
[25] R. Evarestov and A. Bandura, IOP Conf. Ser.: Mater. Sci. Eng. **23**, 012013 (2011).
[26] S. Piskunov and E. Spohr, J. Phys. Chem. Lett. **2**, 2566–2570 (2011).
[27] O. Lisovski, S. Piskunov, Y. F. Zhukovskii, and J. Ozolins, IOP Conf. Ser.: Mater. Sci. Eng. **38**, 012057 (2012).
[28] Y. C. Nah, I. Paramasivam, and P. Schmuki, ChemPhysChem **11**, 2698–2713 (2010).
[29] R. Dovesi, V. R. Saunders, C. Roetti, R. Orlando, C. M. Zicovich-Wilson, F. Pascale, B. Civalleri, K. Doll, N. M. Harrison, I. J. Bush, Ph. D'Arco, and M. Llunell, CRYSTAL09 User's Manual, University of Torino, Torino, 2009, http://www.crystal.unito.it/.
[30] S. Piskunov, E. Spohr, T. Jacob, E. A. Kotomin, and D. E. Ellis, Phys. Rev. B **76**, 012410 (2007).
[31] S. Piskunov, A. Gopeyenko, E. A. Kotomin, Y. F. Zhukovskii, and D. E. Ellis, Comput. Mater. Sci. **41**, 195–201 (2007).
[32] Y. F. Zhukovskii, E. A. Kotomin, S. Piskunov, and D. E. Ellis, Solid State Commun. **149**, 1359–1362 (2009).

[33] C. Adamo and V. Barone, J. Chem. Phys. **110**, 6158–6170 (1999).
[34] M. Ernzerhof and G. E. Scuseria, J. Chem. Phys. **110**, 5029–5036 (1999).
[35] A. D. Becke, J. Chem. Phys. **98**, 5648–5652 (1993).
[36] P. Durand and J. Barthelat, Theor. Chim. Acta **38**, 283 (1975).
[37] J. Barthelat and P. Durand, Gazz. Chim. Ital. **108**, 225 (1978).
[38] J. Barthelat, P. Durand, and A. Serafini, Mol. Phys. **33**, 159 (1977).
[39] P. J. Hay and W. R. Wadt, J. Chem. Phys. **82**, 299–310 (1984).
[40] S. Piskunov, E. Heifets, R. I. Eglitis, and G. Borstel, Comput. Mater. Sci. **29**, 165–178 (2004).
[41] H. J. Monkhorst and J. D. Pack, Phys. Rev. B **13**, 5188–5192 (1976).
[42] R. Haubner, M. Wilhelm, R. Weissenbacher, and B. Lux, in: ''High Performance Non-Oxide Ceramics II'', Structure and Bonding, Vol. 102 (Springer, Berlin, Heidelberg, New York, 2002), pp. 1–45.
[43] D. A. Evans, A. G. McGlynn, B. M. Towlson, M. Gunn, D. Jones, T. E. Jenkins, R. Winter, and N. R. J. Poolton, J. Phys.: Condens. Matter **20**, 075233 (2008).
[44] A. N. Enyashin and G. Seifert, Phys. Status Solidi B **242**, 1361–1370 (2005).
[45] A. M. Ferrari, D. Szieberth, C. M. Zicovich-Wilson, and R. Demichelis, J. Phys. Chem. Lett. **1**, 2854–2857 (2010).

